


# Real-Space Characterization of Cavity-Coupled Waveguide Systems in Hypersonic Phononic Crystals

D. Hatanaka\* and H. Yamaguchi

*NTT Basic Research Laboratories, NTT Corporation, Atsugi-shi, Kanagawa 243-0198, Japan*

 (Received 12 September 2019; revised manuscript received 11 December 2019; accepted 8 January 2020; published 5 February 2020)

A phononic crystal formed in a suspended membrane provides full confinement of hypersonic waves and thus realizes a range of chip-scale manipulations. In this paper, we demonstrate mode-resolved real-space characterization of mechanical-vibration properties in cavities and waveguide systems. Multiple resonant modes in various designed cavities are independently characterized, and wavelength-scale high- $Q$  resonances up to  $Q = 4200$  under atmospheric conditions are confirmed. This also reveals that the waveguide allows us to observe mode-resolved wave transmission and thereby drive evanescently coupled cavities. The methods offer a significant tool with which to build compact and low-power microwave phononic circuitry for applications to signal processing and hybrid quantum systems.

DOI: [10.1103/PhysRevApplied.13.024005](https://doi.org/10.1103/PhysRevApplied.13.024005)

## I. INTRODUCTION

The on-chip control of acoustic phonons at microwave frequencies, namely hypersound, has been essential for a wide range of applications such as sensing for biochemical detection [1], analog signal processing [2], and wireless communications [3]. Moreover, this has also realized an alternative way to drive other degrees of freedom such as photons [4–16], electrons [17–20], and spins [21–28], thus giving rise to the development of alternative hybrid architectures. In the above systems, hypersonic vibrations can be exploited to efficiently actuate and modulate these fundamental excitations or particles, and to interconnect information between different subsystems, which offers alternative opportunities in emerging fields such as quantum acoustics [8–15] and spin mechanics [21–28]. It is becoming increasingly important to develop the ability to manipulate such ultrahigh-frequency acoustic phonons and thus develop phononic technology.

A phononic crystal (PnC) is an artificial material consisting of a periodic elastic composite [29–41]. By using such an engineered structure, the dispersion relation and band gap of acoustic waves can be tailored and formed, which enables acoustic propagation to be controlled. For instance, a local modulation in the periodic geometry can create a cavity [36] or a waveguide [33,37–39] sustained by the band gap, which spatially traps or guides acoustic waves, respectively. This PnC concept has been introduced into various micromechanical systems operating at microwave frequencies, including surface-acoustic-wave (SAW)

devices [42,43], suspended nanobeams [6,7,15,16,44], and membranes [38,39,45]. In terms of the scalability of device integration, a suspended PnC membrane is a suitable platform because it can realize both a high quality factor ( $Q$ ) and a small mode volume ( $V_m$ ), leading to low loss and a small device footprint. This also allows us to incorporate various components into a two-dimensional membrane, thus enabling intricate phonon manipulations. However, the key building blocks such as cavities, waveguides, and evanescently coupled structures of them based on PnC membranes have yet to be fully investigated. In particular, the lack of information on the real-space vibration structures of various device geometries prevents the mode structure, volume, and wave number from being precisely determined. Several pioneering papers have reported optical imaging of acoustic waves in hypersonic devices including PnC membranes [33–35,46,47]. Although these results were promising, they did not investigate a PnC-based cavity, a waveguide, or a coupled structure of them and did not perform a systematic characterization of their mechanical dynamics via  $Q$  and  $V_m$  by using optically detected modal shapes. Thus, this difficulty limits the availability of this PnC platform.

In the work presented in this paper, we fabricate and investigate PnC cavities and waveguides built in suspended GaAs membranes. Measuring the spectral responses enables us to find multiple hypersonic resonances in the 0.50–0.58 GHz range, and then their frequencies and  $Q$  factors. Real-space visualization of their vibrations using an optical interferometric technique identifies the modal shapes that allow the mode volumes and wave numbers to be extracted by comparison with a calculation using the finite-element method (FEM). As a result, we

\*daiki.hatanaka.hz@hco.ntt.co.jp

realize a PnC cavity with  $Q = 4200$  and  $V_m = 2.4 \mu\text{m}^3 = 0.18\lambda^2 t$  at 0.5435 GHz in the atmosphere, where  $\lambda$  and  $t$  are the acoustic wavelength and the membrane thickness, respectively. The high  $Q$  and wavelength-scale  $V_m$  are comparable to and smaller than, respectively, those of conventional PnC cavities at room temperature [6,7,36,45]. Furthermore, we fabricate and investigate cavity-waveguide systems where a cavity is evanescently coupled to a waveguide, and show that the over- and undercoupling conditions can be changed by the spatial separation between the cavity and the waveguide. Our results provide useful information for designing cavities and waveguides and for constructing compact and low-power phononic circuitry for optomechanics and spin-mechanics applications.

## II. EXPERIMENTAL SETUP

The device has a GaAs(1.0  $\mu\text{m}$ )/Al<sub>0.7</sub>Ga<sub>0.3</sub>As(3.0  $\mu\text{m}$ ) heterostructure, as shown in Fig. 1(a). A periodic array of

air holes is patterned in the GaAs layer, which is suspended by sacrificially etching the Al<sub>0.7</sub>Ga<sub>0.3</sub>As layer through the holes with diluted hydrofluoric acid [see the left insets in Fig. 1(b)]. A triangular lattice of snowflake-shaped holes [right inset in Fig. 1(b)] is used for the PnC geometry (middle inset) [48], and this gives rise to a complete phononic band gap in the 0.5–0.6 GHz and 0.7–0.8 GHz regions when the micrometer-scale periodicity shown in Fig. 1(c) is adopted. Hypersonic waves are piezoelectrically excited by one of the interdigitated transducers (IDTs) on the sides of the device by applying microwave signals to the transducer. The acoustic waves travel on the surface of the GaAs layer as Rayleigh waves and are then transformed into Lamb waves in the PnC membrane (see Sec. 1 in the Supplemental Material) [49]. The resultant vibrations are measured with a commercially available optical interferometer (Neoark MLD-101) as shown in Fig. 1(d).

To characterize the modal shape of the vibration field in the device, a phase-sensitive imaging setup is used,

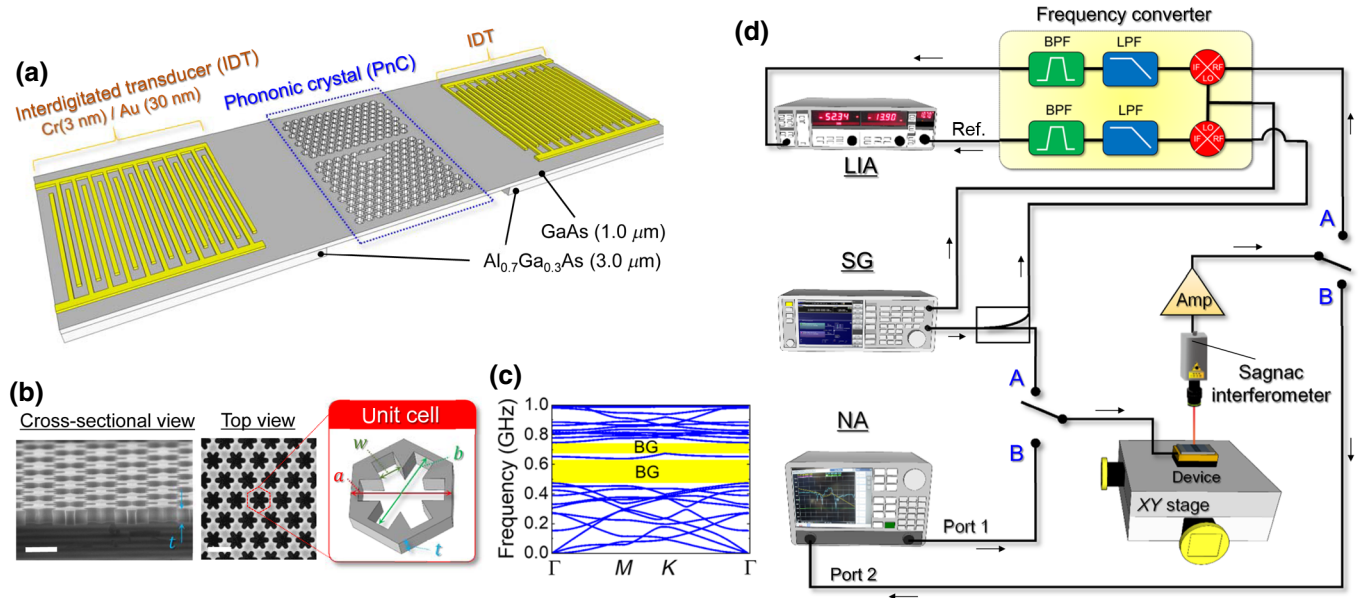


FIG. 1. (a) Schematic illustration of an electromechanical PnC device, in which a two-dimensional phononic shield is formed in a 1.0- $\mu\text{m}$ -thick GaAs membrane by forming a triangular lattice with periodic air holes. IDTs made of Cr(3.0 nm)/Au(30 nm) with 100 finger pairs and  $p = 5.1\text{--}5.9 \mu\text{m}$  are introduced in two parts of the bulk structure, which enable hypersonic waves to be piezoelectrically excited by the application of electromagnetic waves. The Al<sub>0.7</sub>Ga<sub>0.3</sub>As(3  $\mu\text{m}$ ) layer is a sacrificial layer and is selectively etched to form the suspended GaAs membrane. (b) SEM images of a cross section and the top of the PnC lattice are shown in the left and middle insets, where the scale bars are 2 and 4  $\mu\text{m}$ , respectively. A unit cell containing a snowflake-shaped air hole is shown in the right inset, where  $a = 4.0 \mu\text{m}$ ,  $b = 3.4 \mu\text{m}$ ,  $w = 1.0 \mu\text{m}$ , and  $t = 1.0 \mu\text{m}$  are the lattice constant, hole length, hole width, and membrane thickness, respectively. (c) Dispersion relation of the PnC lattice calculated by FEM, which exhibits complete band gaps (BGs) at 0.5–0.6 and 0.7–0.8 GHz, where hypersonic waves cannot propagate. (d) Schematic illustration of measurement setups. Configuration A: one of two signal outputs from a signal generator (SG, Anritsu MG3740A) is used to drive the device, and the other is used as a local oscillator. The signals detected with a Sagnac interferometer (Neoark, MLD-101) are down-converted in a frequency converter, where the signals are mixed with the local-oscillator signal to generate an intermediate frequency (IF) at 10.7 MHz. The IF signals, filtered by a low-pass filter and a band-pass filter (LPF, BPF), are measured with a lock-in amplifier (LIA, SRS SR844). A computer-controlled XY stage with a smallest step size of 100 nm performs scanning of a laser over the device, enabling a spatial map of the vibration field to be constructed. Configuration B: a network analyzer (NA, Keysight E5080A) is used to measure the spectral response of  $S_{11}$  in an IDT and optically detected vibration amplitudes in the device.

as shown in measurement configuration A in Fig. 1(d). Intensive research has been done on developing such an ultrahigh-frequency-vibration imaging system [46,47,50], and, in the present work, we use a system based on a Sagnac interferometer which is described in detail by Hashimoto *et al.* [50]. Here, microwaves from a signal generator are used to drive the device, and the resultant output signal is down-converted by a frequency converter, followed by a lock-in amplifier. The spatial evolution of the output signal is investigated to laterally scan a laser over the device using a movable  $XY$  stage with a resolution of less than  $1 \mu\text{m}$ . To investigate the spectral response of the device, measurement configuration B is used, where the excitation and detection of the signal are carried out by a network analyzer, as shown in Fig. 1(d). All experiments in this work are performed in the atmosphere.

### III. RESULTS

#### A. Line-defect cavities

First, we characterize resonance modes in a PnC cavity, which is formed by removing holes from a periodic lattice, as the simplest and most basic device structure. Figure 2(a) shows an L3 cavity, from which three holes in a line are missing. Such a line-defect cavity has the potential to enable hypersonic waves at frequencies within the band gap to be confined in the defect. To confirm this possibility, the spectral response of the L3 cavity is measured under piezoelectric excitation from one of the IDTs. The electromagnetic-wave reflection from the IDT ( $S_{11}$ ) exhibits distinct absorption around 0.53 GHz, as shown in the top panel of Fig. 2(b), indicating that the injected energy is converted to a SAW (Rayleigh wave) by the piezoelectric effect. The operational bandwidth ( $f_{\text{SAW}}$ ) of the IDT can be estimated from  $f_{\text{SAW}} = v_{\text{GaAs}}/p = 0.521 \text{ GHz}$ , where  $v_{\text{GaAs}}$  and  $p$  are the SAW velocity of GaAs (2867 m/s [51]) and the periodic pitch of the IDT ( $5.5 \mu\text{m}$ ), respectively. The slight deviation from the experimental value might be due to the different SAW velocity of the  $\text{Al}_{0.7}\text{Ga}_{0.3}\text{As}$  underlayer [51]. The multiple small interferometric fringes appearing in  $S_{11}$  are caused by the reflection of SAWs from the device edge [see also Fig. 6(c)]. The cavity dynamics are evaluated from optically detected displacement amplitudes ( $A_{\text{opt}}$ ) with the focal point on an antinode of the vibration, as shown in the bottom panel of Fig. 2(b), which reveals a well-defined sharp peak around 0.529 GHz. By fitting a Lorentz curve to the peak as shown in the inset, the  $Q$  factor can be estimated as  $Q = 3700$ . Real-space mapping is performed by scanning the laser spot position over the cavity at 0.5293 GHz, and the amplitude and phase components obtained are plotted in the top and bottom panels of Fig. 2(c), respectively. The vibration is well localized in the defect area and shows a mode shape that provides experimental proof of the usability of the snowflake PnC

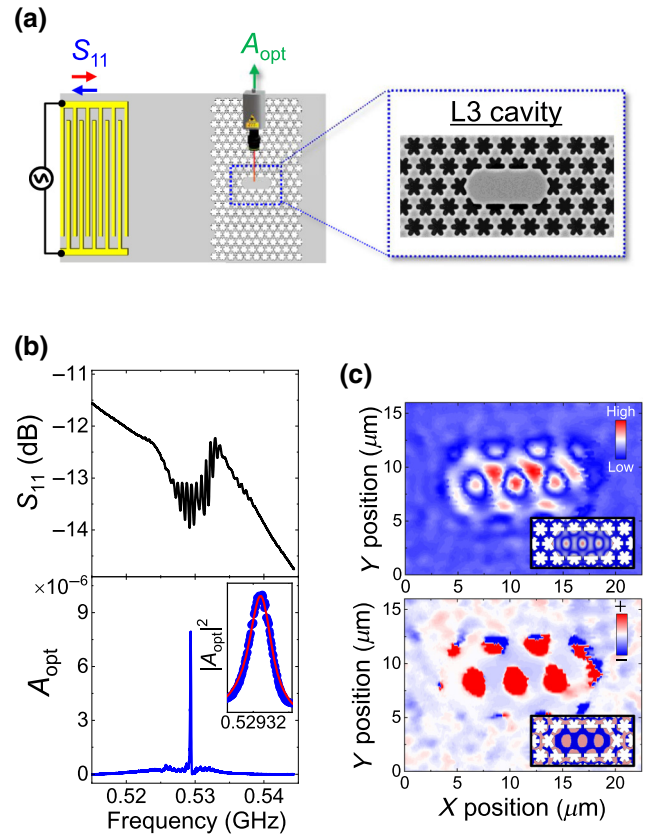


FIG. 2. (a) Measurement setup for a line-defect (L3) cavity. The application of electromagnetic waves to an IDT electrode excites SAWs (Rayleigh waves) through the piezoelectric effect. The acoustic waves are sent into the cavity, which is surrounded by a PnC lattice. The resultant vibration spectrum is probed using an optical interferometer under atmospheric conditions. (b) Spectral response of the electrical reflection from the IDT ( $S_{11}$ , top panel), and optically measured transmission ( $A_{\text{opt}}$ , bottom panel) of the device. The inset shows the enlarged spectral response of  $|A_{\text{opt}}|^2$ , and the red solid line shows a fitted curve. (c) Real-space maps of the amplitude and phase of vibration at 0.5293 GHz in top and bottom panels, respectively; the corresponding mode profiles simulated by FEM are also shown in the insets.

shield in our experiments. The resultant amplitude and phase distributions of this mode can be predicted by FEM calculations using COMSOL MULTIPHYSICS, as shown in the insets of Fig. 2(c). The simulations indicate that this mode is induced by an asymmetric Lamb wave. This also allows the effective mode volume to be calculated by integrating the vibration energy over the entire membrane as  $V_m = \int d^2r [|q(r)|/\max(|q(r)|)]^2 t = 8.1 \mu\text{m}^3 = 0.63\lambda^2 t$ , where  $q(r)$  is the calculated mode-profile displacement. In contrast, the absolute displacement amplitude cannot be experimentally determined, due to the limitations of this optical detection method and the unmeasurable thermomechanical noise in the cavity. Thus, the results indicate that the line-defect cavity formed in the snowflake PnC lattice

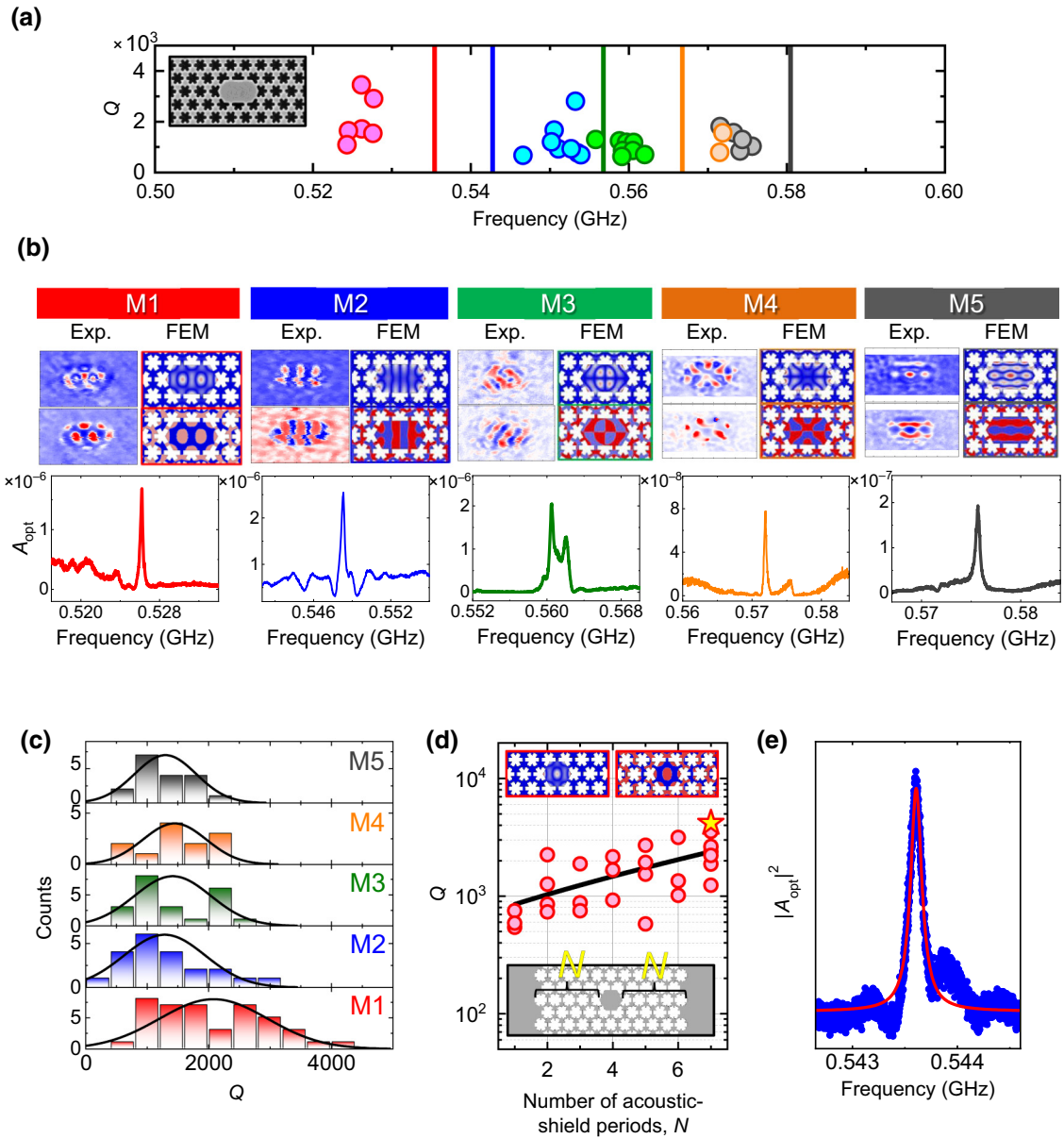


FIG. 3. (a) Resonance frequencies and  $Q$  factors of multimodal L2 cavities M1, M2, M3, M4, and M5 with  $N = 5-7$ , plotted as red, blue, green, orange and gray circles, respectively. The resonance frequencies are numerically calculated, including the anisotropic elastic constants, and shown by solid lines. Each color of the solid lines corresponds to a resonant mode as shown in (b). (b) The top panels show the amplitude (upper part of panel) and phase (lower part) distributions of the mode profiles of M1–M5, experimentally and numerically obtained, as shown in the left and right parts of the panels, respectively. The experimental spectral response of each mode is shown in the bottom panel. The M3 mode shows splitting into two peaks because of undesired contamination or because of imperfections in fabrication. (c) Histogram of  $Q$  factors for M1–M5 and fitted curves using a Gaussian distribution function, shown in the panels from bottom to top. The experimental data are taken from L1–L4 cavities with  $N = 5-7$ . (d) Dependence of  $Q$  factor of the M1 mode in an L1 cavity on number of acoustic-shield periods  $N$ . The solid black line is an exponential fit. The mode profiles of the amplitude and phase are depicted in the left and right panels, respectively, of the top inset. A schematic illustration of the device is shown in the bottom inset, where  $N$  is defined. (e) Spectral response of the L1 cavity with  $N = 7$  (blue), denoted by a star in (d), and a fitted curve (red), showing the highest  $Q$ , equal to 4200.

realizes wavelength-scale lateral confinement of hypersonic vibrations and a  $Q$  factor as high as that reported in conventional hypersonic cavities at room temperature [6,7,42,43,45].

In this way, the spectral response of five types of L $x$  cavity ( $x = 1-5$ ) is investigated over a broad frequency span of 0.5–0.6 GHz. Finally, we observe multiple hypersonic resonances in each cavity and also the corresponding

frequencies and  $Q$ s. The  $Q$ s obtained for the L2 cavity are plotted with respect to the resonant frequency in Fig. 3(a). A total of five different modes can be found thanks to the real-space mapping measurements, labeled M1–M5 and denoted by circles of different colors; their modal shapes are shown in Fig. 3(b). By repeating the same measurements with several samples, we confirm that each mode shows a similar resonant frequency. To support the findings, FEM simulations are conducted and reveal that the elastic anisotropy of the GaAs crystal plays an essential role in explaining the mode frequencies. Note that the calculated mode frequencies can predict the experimental ones when the elastic anisotropy is considered, as denoted by the solid lines [52], thus indicating that the devices can be well fabricated so as to reproduce the original designs. Similar results are also obtained for L1, L3, and L4 cavities (see Sec. 2 in the Supplemental Material) [49].

The  $Q$  factor, describing energy loss, is an essential parameter for evaluating the characteristics of a cavity. All the  $Q$ s obtained experimentally from the L1–L5 cavities are classified as corresponding to different modes (M1–M5) based on the real-space mapping results, as shown in Fig. 3(c). Although there is a finite variation in the  $Q$ s for each mode, the M1 mode is likely to show a higher  $Q$  factor (average  $Q_{\text{cav}} = 2080$ ) than the others ( $Q_{\text{cav}} = 1286\text{--}1447$ ). Next, we focus on the M1 mode in an L1 cavity and investigate the  $Q$  factor for various numbers of acoustic-shield periods ( $N$ ), as shown in Fig. 3(d). The  $Q$  values increase monotonically with increasing  $N$  and, in

particular, the highest  $Q_{\text{cav}}$ , equal to 4200, and the smallest  $V_m$ , equal to  $2.4 \mu\text{m}^3 = 0.18\lambda^2 t$ , in this work are found for  $N = 7$ , denoted by a filled star, and its spectral response is shown in Fig. 3(e). However, the measured increment of  $Q$  with  $N$  is much less than that predicted by FEM calculations (see Sec. 3 in the Supplemental Material) [49]. Therefore, there are other major dissipation sources. Material losses such as thermoelastic damping and a surface two-level system (TLS) can possibly induce dissipation [53], whereas air damping is not significant, because we confirm that the  $Q$  values do not change in a vacuum. According to a previous report on GaAs optomechanical systems operating at 0.26 GHz by Hamoumi *et al.* [54], the major part of the dissipation is caused by a GaAs TLS at room temperature. It ranges from 50 to 100 kHz and is of the same order of magnitude as that of our cavities. Thus, internal sources of dissipation such as a TLS may also be dominant in our devices, which is confirmed by the dispersion in the  $Q$  values for a given  $N$  in Fig. 3(d) due to device-by-device variation in the TLS. Surface treatment during or after fabrication could help to increase the  $Q$  factors.

## B. Line-defect waveguide

Secondly, an acoustic waveguide is realized by creating a line defect in the periodic lattice, where hypersonic waves are guided while being sustained by the band gap. Figure 4(a) shows a PnC waveguide formed by simply

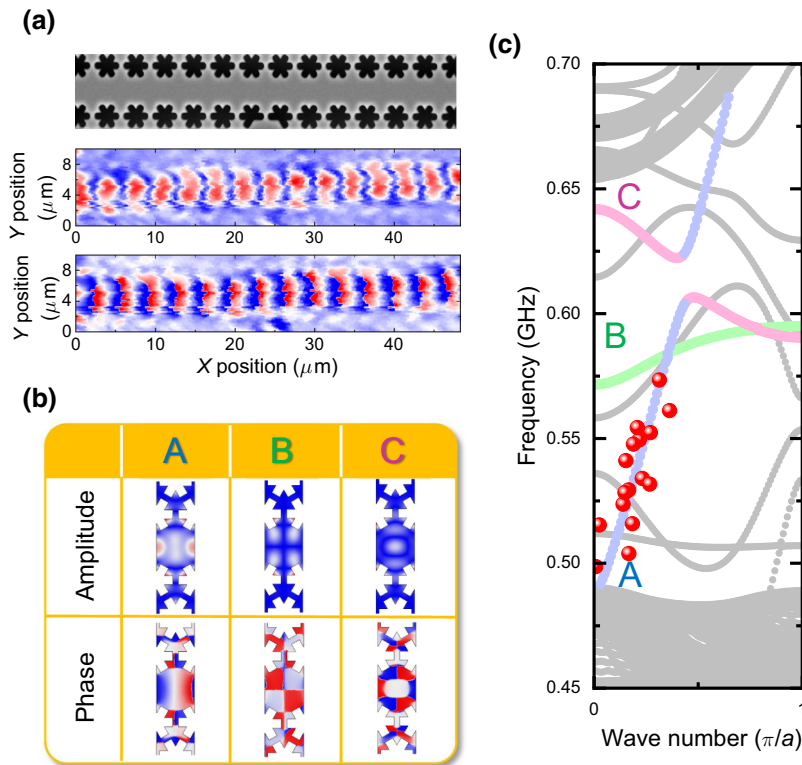


FIG. 4. (a) SEM image of a line-defect waveguide (top), and spatial distributions of its amplitude (middle) and phase (bottom) at 0.573 GHz. (b) Mode profiles of guided modes A, B, and C simulated by FEM. (c) Dispersion relation of a line-defect waveguide in a snowflake-based PnC. The FEM calculation shows multiple guided modes in the band gap from 0.50 to 0.65 GHz, where several asymmetric Lamb modes (light blue, green, and red lines) and Love modes (gray line) exist simultaneously. The phononic branches of the Lamb modes are labeled A, B, and C, which correspond to the mode profiles shown in (b). The dispersion relation is also experimentally estimated from the real-space mapping results, as denoted by solid red circles.

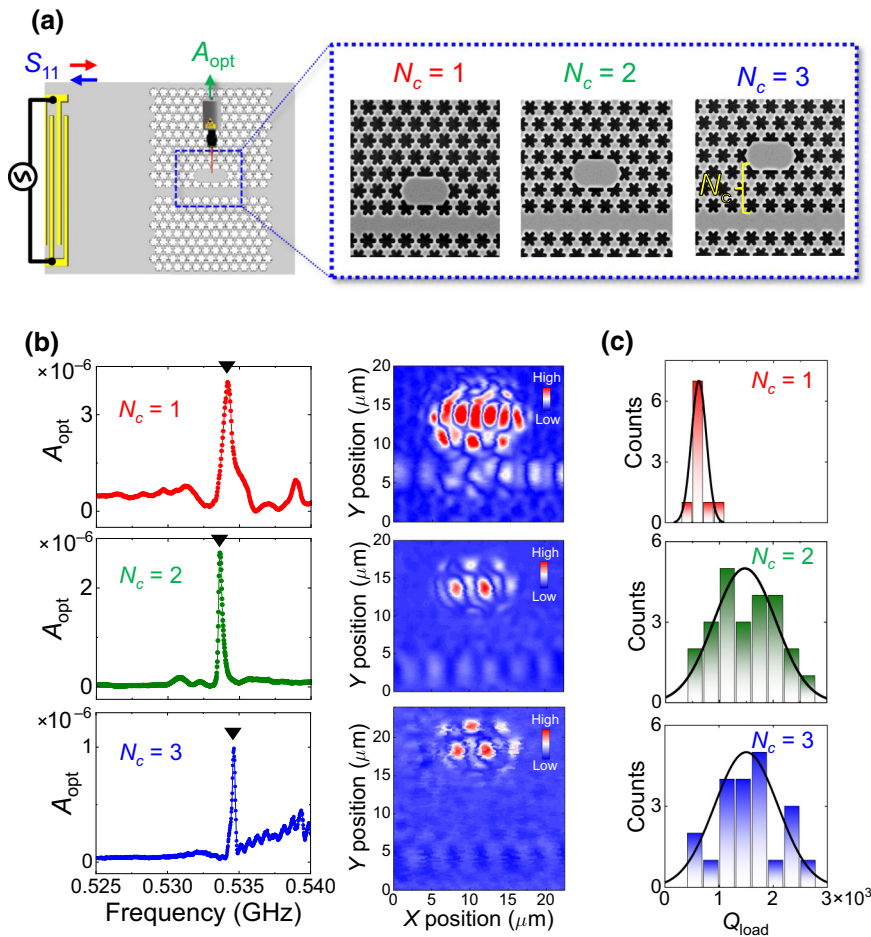


FIG. 5. (a) Measurement setup for cavity-waveguide structures, where an L2 cavity is side-coupled to a line-defect waveguide with a spatial separation between the cavity and the waveguide  $N_c = 1, 2$ , and 3. These structures are shown in the left, middle, and right insets, respectively. (b) Spectral responses of transmission  $A_{opt}$  for L2 cavities in the configurations  $N_c = 1$  (top), 2 (middle), and 3 (bottom). The observed resonance peaks originate from the M1 mode (black triangles), and are confirmed by amplitude real-space mapping as shown in the right insets. (c) Histograms of loaded  $Q$  factors  $Q_{load}$  of the L2 cavity system in these configurations.

removing one row of holes from the triangular lattice. An incident Lamb wave excited by an IDT can be confined in the line defect and spatially guided, as shown in the bottom panels of Fig. 4(a). This waveguiding mode has one vibration antinode in the center of the waveguide, and it is calculated and shown as mode profile A in Fig. 4(b). The visualized spatial evolution of the amplitude and phase provides wave-number information about the waves. In this way, the dispersion relation for acoustic propagation in the waveguide can be constructed by collecting these data at various frequencies from 0.50 to 0.58 GHz, and this relation is plotted as solid red circles in Fig. 4(c). Also shown is the dispersion relation calculated by use of the FEM, where phononic bands for Lamb waves (out-of-plane displacement) and Love waves (in-plane displacement) are depicted in color (light blue, green, and red) and gray, respectively. Because of the limitations of our optical detection method, we can detect only out-of-plane Lamb waves, and thus a waveguiding mode in branch A can be resolved in the above frequency range. Additional branches B and C are available, as depicted in light green and red, and can support waveguiding modes containing two and three antinodes, respectively, which can be seen in Fig. 4(b). These modes are not observed, due to their

frequencies being beyond the excitation range of the IDTs. In particular, branch A interacts branch C, showing anti-crossing around 0.61 GHz, but not with branch B, due to the parity difference between odd and even modal shapes. It should be mentioned that Love waves could also be detectable if the measurement configuration was changed, e.g., by injecting a laser beam at a nonnormal angle or by focusing a laser spot around a waveguide side edge.

### C. Cavity-waveguide systems

The use of a waveguide enables us to spatially address distant cavities. Such a cavity-waveguide coupled geometry is fundamental to the construction of integrated phononic circuits as shown in the left inset in Fig. 5(a). Here, we use L2 cavity-waveguide systems with various cavity-waveguide separations  $N_c = 1, 2$ , and 3 between these two components, as shown in the left, middle, and right panels, respectively, of Fig. 5(a), and measure the spectral response of the cavities, as shown in the left panels of Fig. 5(b). All the cavities exhibit a well-defined resonance peak around 0.534 GHz, which is indeed sustained by the M1 mode, as confirmed by the right panels in Fig. 5(b). The average  $Q$  factors for these three

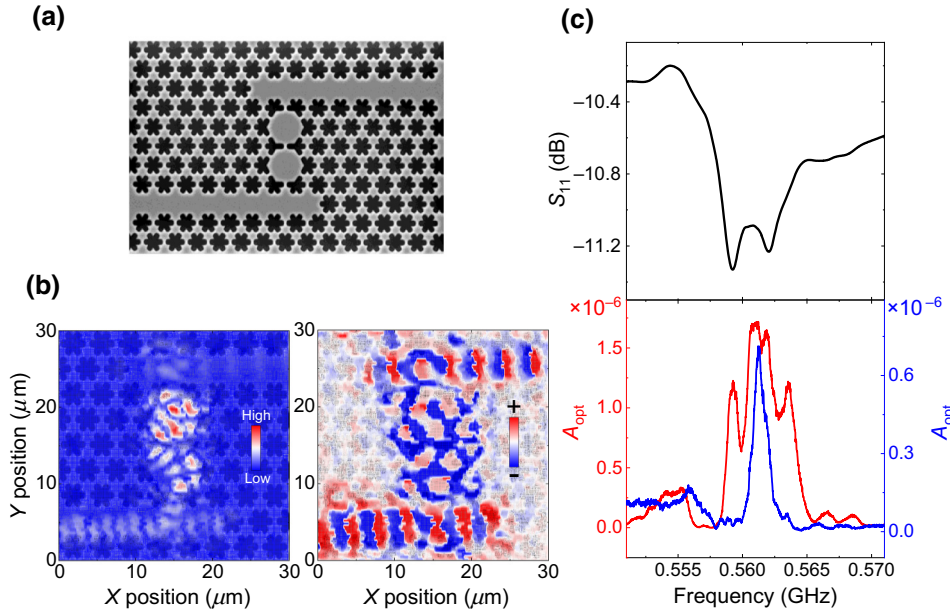


FIG. 6. (a) SEM image of a PnC-based microwave filter, where two L1 cavities are sandwiched between waveguides. The bottom and top waveguides are used as input and output waveguides, respectively. (b) Spatial distribution of the amplitude (left) and phase (right) of hypersonic transmission at 0.561 GHz. (c)  $S_{11}$  (top) and  $A_{opt}$  (bottom) spectra measured at the input (red line) and output (blue line) waveguide.

configurations are examined, which reveals that the loaded  $Q$  factor  $Q_{load}$  of the cavity with  $N_c = 1$  is 600 and is lower than that for the others: for  $N_c = 2$ ,  $Q_{load} = 1474$ , and for  $N_c = 3$ ,  $Q_{load} = 1454$ , as shown in Fig. 5(c). On the other hand,  $Q_{load}$  is invariant between  $N_c = 2$  and  $N_c = 3$ . Briefly, the dissipation of a cavity in such a cavity-waveguide system is given by

$$Q_{load}^{-1} = Q_{cav}^{-1} + Q_{wg}^{-1}, \quad (1)$$

where  $Q_{wg}$  is the quality factor for dissipation through the waveguide. From the experimental results in Fig. 3(c), indicating the intrinsic  $Q$  factor of the cavity in the M1 mode ( $Q_{cav} = 2080$ ),  $Q_{wg}$  can be extracted as 843, 5059, and 4831 for the  $N_c = 1, 2$ , and 3 configurations, respectively. Therefore, the cavity-waveguide system with  $N_c = 1$  is in an overcoupling regime, namely  $Q_{wg}^{-1} > Q_{cav}^{-1}$ , where energy dissipation through the waveguide is dominant; in other words, it enables the cavity to be efficiently driven. On the other hand, the other configurations, with  $N_c = 2$  and 3, realize an undercoupling regime,  $Q_{wg}^{-1} < Q_{cav}^{-1}$ , where the intrinsic cavity dissipation is dominant, and thus the cavity can be excited while retaining its intrinsic  $Q_{cav}$ . Thus, the coupling condition between the cavity and the waveguide can be altered by changing the spatial separation, and the transition from over- to undercoupling can be found between  $N_c = 1$  and 2.

This cavity-waveguide structure is a building block for the construction of phononic circuits. For instance, an acoustic microwave filter composed of cavities sandwiched between two waveguides is demonstrated, as shown in Fig. 6(a). Hypersonic waves at 0.561 GHz excited by an IDT are injected into the input waveguide (bottom) and then propagate to the output waveguide (top) through the cavities, which can be visualized as shown

in Fig. 6(b). The resultant waves in the output waveguide are filtered by the cavity resonance, as shown in Fig. 6(c), the bandwidth of which is approximately 1 MHz as determined by the  $Q$  factor. This bandpass region is narrower than that of the input waveguide, which is approximately 5 MHz, resulting from the spectral response of the IDT. In conventional microwave filters based on SAW devices, the bandwidth is determined by the number of IDT electrodes. Namely, a narrower passband can be realized with a larger number of electrodes on a SAW filter. Briefly, 500 electrode finger pairs are needed to fabricate a 1-MHz bandpass filter that has an IDT with a length of several millimeters. On the other hand, a filter based on a PnC membrane realizes a high  $Q$  and a low  $V_m$ , and so it can be band-narrowing and be compact on the scale of the wavelength. By optimizing IDTs with highly piezoelectric materials such as  $\text{LiNbO}_3$ , the finger-pair number can be reduced, and thus the entire device size can be made much smaller, with a length of several tens of micrometers. Additionally, the bandwidth and spectral position are adjustable by engineering the cavity geometry. For instance, a broad passband can also be realized by forming a linear cavity array. Moreover, the propagation loss can be suppressed by optimizing the coupling geometry and modal shapes of the cavity and the waveguide. This hypersonic PnC holds promise as a platform on which to develop functional and compact phononic circuits.

#### IV. CONCLUSION

In conclusion, hypersonic PnC devices in a suspended GaAs membrane are demonstrated, and their mechanical-vibration properties are investigated with a real-space mapping technique. Experiments on real-space characterization reveal that multiple hypersonic resonances are

available in various line-defect cavities, and, in particular, a high quality factor  $Q = 4200$  and a small mode volume  $V_m = 0.18\lambda^2 t$  are realized in an L1 cavity. Additionally, the dispersion relation of a waveguide is constructed by acquiring the amplitude and phase of the spatial information, clarifying the possibility of efficient and chip-scale hypersonic waveguiding. Moreover, this waveguide allows us to drive a cavity remotely, and the driving efficiency can be changed by adjusting the coupling geometry. The PnC architecture enables the realization of compact and functional phononic circuitry, thus increasing the availability of acoustic phonons in conventional signal-processing applications as well as in optomechanics and spin mechanics.

### ACKNOWLEDGMENTS

We thank Dr. T. Tamamura, Dr. M. Ono, Dr. S. Sasaki, and Dr. Y. Harada for their support and helpful comments on device fabrication. We are also grateful to Dr. R. Ohta and Dr. M. Asano for fruitful discussions on the FEM calculations. This work is supported by a MEXT Grant-in-Aid for Scientific Research on Innovative Areas “Science of hybrid quantum systems” (Grants No. JP15H05869 and No. JP15K21727). We acknowledge stimulating discussion at a meeting of the Cooperative Research Project of the Research Institute of Electrical Communication, Tohoku University.

- 
- [1] K. Lange, B. E. Rapp, and M. Rapp, Surface acoustic wave biosensors: A review, *Anal. Bioanal. Chem.* **391**, 1509 (2008).
- [2] D. Morgan, *Surface Acoustic Wave Filters, With Applications to Electronic Communications and Signal Processing* (Academic Press, Oxford, 2007).
- [3] K.-Y. Hashimoto, *Surface Acoustic Wave Devices in Telecommunications* (Springer, Berlin, 2000).
- [4] D. A. Fuhrmann, S. M. Thon, H. Kim, D. Bouwmeester, P. M. Petroff, A. Wixforth, and H. J. Krenner, Dynamic modulation of photonic crystal nanocavities using gigahertz acoustic phonons, *Nat. Photon.* **5**, 605 (2011).
- [5] S. A. Tadesse and M. Li, Sub-optical wavelength acoustic wave modulation of integrated photonic resonators at microwave frequencies, *Nat. Commun.* **5**, 5402 (2014).
- [6] K. C. Balram, M. I. Davanco, J. D. Song, and K. Srinivasan, Coherent coupling between radiofrequency, optical and acoustic waves in piezo-optomechanical circuits, *Nat. Photon.* **10**, 346 (2016).
- [7] K. Fang, M. H. Matheny, X. Luan, and O. Painter, Optical transduction and routing of microwave phonons in cavity-optomechanical circuits, *Nat. Photon.* **10**, 489 (2016).
- [8] M. V. Gustafsson, P. V. Santos, G. Johansson, and P. Delsing, Propagating phonons coupled to an artificial atom, *Science* **346**, 207 (2014).
- [9] Y. Chu, P. Kharel, W. H. Renninger, L. D. Burkhardt, L. Frunzio, P. T. Rakich, and R. J. Schoelkopf, Quantum acoustics with superconducting qubits, *Science* **358**, 199 (2017).
- [10] R. Manenti, A. F. Kockum, A. Patterson, T. Behrle, J. Rahamin, G. Tancredi, F. Nori, and P. J. Leek, Circuit quantum acoustodynamics with surface acoustic waves, *Nat. Commun.* **8**, 975 (2017).
- [11] A. Noguchi, R. Yamazaki, Y. Tabuchi, and Y. Nakamura, Qubit-assisted Transduction for a Detection of Surface Acoustic Waves near the Quantum Limit, *Phys. Rev. Lett.* **119**, 180505 (2017).
- [12] Y. Chu, P. Kharel, T. Yoon, L. Frunzio, P. T. Takich, and R. J. Schoelkopf, Creation and control of multi-phonon fock states in a bulk acoustic-wave resonator, *Nature* **563**, 666 (2018).
- [13] K. J. Satzinger, Y. P. Zhong, H.-S. Chang, G. A. Peairs, A. Bienfait, M.-H. Chou, A. Y. Cleland, C. R. Conner, . Dumur, J. Grebel, *et al.*, Quantum control of surface acoustic-wave phonons, *Nature* **563**, 661 (2018).
- [14] L. R. Sletten, B. A. Moores, J. J. Viennot, and K. W. Lehnert, Resolving Phonon Fock States in a Multimode Cavity with a Double-Slit Qubit, *Phys. Rev. X* **9**, 021056 (2019).
- [15] P. Arrangoiz-Arriola, E. A. Wollack, M. Pechal, J. D. Witmer, J. T. Hill, and A. H. Safavi-Naeini, Coupling a Superconducting Quantum Circuit to a Phononic Crystal Defect Cavity, *Phys. Rev. X* **8**, 031007 (2018).
- [16] M. Kalaei, M. Mirhosseini, P. B. Dieterle, M. Peruzzo, J. M. Fink, and O. Painter, Quantum electromechanics of a hypersonic crystal, *Nat. Nanotechnol.* **14**, 334 (2019).
- [17] W. J. M. Naber, T. Fujisawa, H. W. Liu, and W. G. van der Wiel, Surface-Acoustic-Wave-Induced Transport in a Double Quantum dot, *Phys. Rev. Lett.* **96**, 136807 (2006).
- [18] M. V. Gustafsson, T. Aref, A. F. Kockum, M. K. Ekstrom, G. Johansson, and P. Delsing, Local probing of propagating acoustic waves in a gigahertz echo chamber, *Nat. Phys.* **8**, 338 (2012).
- [19] J. C. H. Chen, Y. Sato, R. Kosaka, M. Hashisaka, K. Muraki, and T. Fujisawa, Enhanced electron-phonon coupling for a semiconductor charge qubit in a surface phonon cavity, *Sci. Rep.* **5**, 15176 (2015).
- [20] Y. Sato, J. C. H. Chen, M. Hashisaka, K. Muraki, and T. Fujisawa, Two-electron double quantum dot coupled to coherent photon and phonon fields, *Phys. Rev. B* **96**, 115416 (2017).
- [21] M. Weiler, L. Dreher, C. Heeg, H. Huebl, R. Gross, M. S. Brandt, and S. T. B. Goennenwein, Elastically Driven Ferromagnetic Resonance in Nickel Thin Films, *Phys. Rev. Lett.* **106**, 117601 (2011).
- [22] M. Weiler, H. Huebl, F. S. Goerg, F. D. Czeschka, R. Gross, and S. T. B. Goennenwein, Spin Pumping with Coherent Elastic Waves, *Phys. Rev. Lett.* **108**, 176601 (2012).
- [23] H. Sanada, Y. Kunihashi, H. Gotoh, K. Onomitsu, M. Kohda, J. Nitta, P. V. Santos, and T. Sogawa, Manipulation of mobile spin coherence using magnetic-field-free electron spin resonance, *Nat. Phys.* **9**, 280 (2011).
- [24] L. Thevenard, C. Gourdon, J. Y. Prieur, H. J. von Bardeleben, S. Vincent, L. Becerra, L. Largeau, and J.-Y. Duquesne, Surface-acoustic-wave-driven ferromagnetic resonance in (Ga, Mn)(As, P) epilayers, *Phys. Rev. B* **90**, 094401 (2014).
- [25] D. Labanowski, V. P. Bhallamudi, Q. Guo, C. M. Purser, B. A. McCullian, P. C. Hammel, and S. Salahuddin,



- Voltage-driven, local, and efficient excitation of nitrogen-vacancy centers in diamond, *Sci. Adv.* **4**, eaat6574 (2018).
- [26] D. Kobayashi, T. Yoshikawa, M. Matsuo, R. Iguchi, S. Maekawa, E. Saitoh, and Y. Nozaki, Spin Current Generation Using a Surface Acoustic Wave Generated via Spin-Rotation Coupling, *Phys. Rev. Lett.* **119**, 077202 (2017).
- [27] D. A. Golter, T. Oo, M. Amezcu, I. Lekavicius, K. A. Stewart, and H. Wang, Coupling a Surface Acoustic Wave to an Electron Spin in Diamond via a Dark State, *Phys. Rev. X* **6**, 041060 (2016).
- [28] S. J. Whiteley, G. Wolfowicz, C. P. Anderson, A. Bourassa, H. Ma, M. Ye, F. Koolstra, K. J. Satzinger, M. V. Holt, F. J. Heremans, *et al.*, Spin-phonon interactions in silicon carbide addressed by gaussian acoustics, *Nat. Phys.* **15**, 490 (2019).
- [29] M. Maldovan, Sound and heat revolutions in phononics, *Nature* **503**, 209 (2013).
- [30] V. Narayanamurti, H. L. Störmer, M. A. Chin, A. C. Gosard, and W. Wiegmann, Selective Transmission of High-Frequency Phonons by a Superlattice: The “dielectric” Phonon Filter, *Phys. Rev. Lett.* **43**, 2012 (1979).
- [31] R. Martínez-Sala, J. Sancho, J. V. Sánchez, V. Gómez, J. Llinares, and F. Meseguer, Sound attenuation by sculpture, *Nature* **378**, 241 (1995).
- [32] S. Benchabane, A. Khelif, J.-Y. Rauch, L. Robert, and V. Laude, Evidence for complete surface wave band gap in a piezoelectric phononic crystal, *Phys. Rev. E* **73**, 065601(R) (2006).
- [33] S. Benchabane, O. Gaiñe, G. Ulliac, R. Sault, Y. Achaoui, and V. Laude, Observation of surface-guided waves in holey hypersonic phononic crystal, *Appl. Phys. Lett.* **98**, 171908 (2011).
- [34] M. Gorisse, S. Benchabane, G. Teissier, C. Billard, A. Reinhardt, V. Laude, E. Defaÿ, and M. Aid, Observation of band gaps in the gigahertz range and deaf bands in a hypersonic aluminum nitride phononic crystal slab, *Appl. Phys. Lett.* **98**, 234103 (2011).
- [35] S. Benchabane, O. Gaiñe, R. Sault, G. Ulliac, V. Laude, and K. Kokkonen, Guidance of surface waves in a micron-scale phononic crystal line-defect waveguide, *Appl. Phys. Lett.* **106**, 081903 (2015).
- [36] S. Mohammadi, A. A. Eftekhar, W. D. Hunt, and A. Adibi, High- $Q$  micromechanical resonators in a two-dimensional phononic crystal slab, *Appl. Phys. Lett.* **94**, 051906 (2009).
- [37] P. H. Otsuka, K. Nanri, O. Matsuda, M. Tomoda, D. M. Profunser, I. A. Veres, S. Danworaphong, A. Khelif, S. Benchabane, V. Laude, *et al.*, Broadband evolution of phononic-crystal-waveguide eigenstates in real- and  $k$ -spaces, *Sci. Rep.* **3**, 3351 (2013).
- [38] R. Pourabolghasem, R. Dehghanasiri, A. A. Eftekhar, and A. Adibi, Waveguiding Effect in the Gigahertz Frequency Range in Pillar-based Phononic-Crystal Slabs, *Phys. Rev. Appl.* **9**, 014013 (2018).
- [39] M. G. Baboly, C. M. Reinke, B. A. Griffin, I. El-Kady, and Z. C. Leseman, Acoustic waveguiding in a silicon carbide phononic crystals at microwave frequencies, *Appl. Phys. Lett.* **112**, 103504 (2018).
- [40] D. Hatanaka, I. Mahboob, K. Onomitsu, and H. Yamaguchi, Phonon waveguides for electromechanical circuits, *Nat. Nanotechnol.* **9**, 520 (2014).
- [41] M. Kurosu, D. Hatanaka, K. Onomitsu, and H. Yamaguchi, On-chip temporal focusing of elastic waves in a phononic crystal waveguide, *Nat. Commun.* **9**, 1331 (2018).
- [42] Y. Xu, W. Fu, C. L. Zou, Z. Shen, and H. X. Tang, High quality factor surface Fabry-Perot cavity of acoustic waves, *Appl. Phys. Lett.* **112**, 073505 (2018).
- [43] L. Shao, S. Maity, L. Zheng, L. Wu, A. Shams-Ansari, Y.-I. Sohn, E. Puma, M. N. Gadalla, M. Zhang, C. Wang, *et al.*, Phononic Band Structure Engineering for High- $q$  Gigahertz Surface Acoustic Wave Resonators on Lithium Niobate, *Phys. Rev. Appl.* **12**, 014022 (2019).
- [44] G. S. MacCabe, H. Ren, J. Luo, J. D. Cohen, H. Zhou, A. Sipahigil, M. Mirhosseini, and O. Painter, Phononic bandgap nano-acoustic cavity with ultralong phonon lifetime. arXiv:1901.04129 (2019).
- [45] M. G. Baboly, S. Alaie, C. M. Reinke, I. El-Kady, and Z. C. Leseman, Ultra-high frequency, high  $q$ /volume micromechanical resonators in a planar aln phononic crystal, *J. Appl. Phys.* **120**, 034502 (2016).
- [46] K. Kokkonen and M. Kaivola, Scanning heterodyne laser interferometer for phase-sensitive absolute-amplitude measurements of surface vibrations, *Appl. Phys. Lett.* **92**, 063502 (2008).
- [47] Z. Shen, X. Han, C.-L. Zou, and H. X. Tang, Phase sensitive imaging of 10 GHz vibrations in an aln microdisk resonator, *Rev. Sci. Instrum.* **88**, 123709 (2017).
- [48] A. H. Safavi-Naeini, J. T. Hill, S. Meenehan, J. Chan, S. Gröblacher, and O. Painter, Two-Dimensional Phononic-photonic Band gap Optomechanical Crystal Cavity, *Phys. Rev. Lett.* **112**, 153603 (2014).
- [49] See the Supplemental Material at <http://link.aps.org/supplemental/10.1103/PhysRevApplied.13.024005>. Section 1 shows the spatial evolution of hypersonic waves from an IDT to a line-defect waveguide. Section 2 shows experimental  $Q$  factors as a function of resonant frequency for L1, L3, and L4 cavities. Section 3 shows the FEM simulation results for  $Q$  factors due to a band gap and thermoelastic damping.
- [50] K. Y. Hashimoto, K. Kashiwa, N. Wu, T. Omori, M. Yamaguchi, O. Takano, S. Meguro, and K. Akahane, A laser probe based on a Sagnac interferometer with fast mechanical scan for rf surface and bulk acoustic wave devices, *IEEE Trans. Ultrason. Ferroelect. Freq. Control* **58**, 187 (2011).
- [51] Y. Takagaki, E. Wiebicke, P. V. Santos, R. Hey, and K. H. Ploog, Propagation of surface acoustic waves in a GaAs/AlAs/GaAs heterostructure and micro-beams, *Semicond. Sci. Technol.* **17**, 1008 (2002).
- [52] S. Adachi, GaAs, AlAs, and  $\text{Al}_x\text{Ga}_{1-x}\text{As}$ : Material parameters for use in research and device applications, *J. Appl. Phys.* **58**, R1 (1985).
- [53] A. N. Cleland, *Foundations of Nanomechanics, From Solid-State Theory to Device Applications* (Springer, Berlin, 2003).
- [54] M. Hamoumi, P. E. Allain, W. Hease, E. Gil-Santos, L. Morgenroth, B. Gérard, A. Lemaître, G. Leo, and I. Favero, Microscopic Nanomechanical Dissipation in Gallium Arsenide Resonators, *Phys. Rev. Lett.* **120**, 223601 (2018).